



Defect-free Metal Deposition on Two-dimensional Materials via Inkjet Printing Technology

Item Type	Article
Authors	Zheng, Wenwen;Saiz, Fernan;Shen, Yaqing;Zhu, Kaichen;Liu, Yingwen;McAleese, Clifford;Conran, Ben;Wang, Xiaochen;Lanza, Mario
Citation	Zheng, W., Saiz, F., Shen, Y., Zhu, K., Liu, Y., McAleese, C., ... Lanza, M. (2021). Defect-free Metal Deposition on Two-dimensional Materials via Inkjet Printing Technology. <i>Advanced Materials</i> , 2104138. doi:10.1002/adma.202104138
Eprint version	Post-print
DOI	10.1002/adma.202104138
Publisher	Wiley
Journal	Advanced Materials
Rights	Archived with thanks to Advanced Materials
Download date	2024-04-16 20:13:43
Link to Item	http://hdl.handle.net/10754/673336

DOI:

Article type: Full Paper

Defect-free metal deposition on two-dimensional materials via inkjet printing technology

*Wenwen Zheng, Fernan Saiz, Yaqing Shen, Kaichen Zhu, Yingwen Liu, Clifford McAleese, Ben Conran, Xiaochen Wang, Mario Lanza**

W. Zheng, Y. Shen, Y. Liu,
Institute of Functional Nano and Soft Materials (FUNSOM), Collaborative Innovation Center of Suzhou Nano Science and Technology, Soochow University, 199 Ren-Ai Road, Suzhou 215123, China

K. Zhu
MIND, Department of Electronic and Biomedical Engineering, Universitat de Barcelona, Martí i Franquès 1, E-08028 Barcelona, Spain

Dr. C. McAleese, Dr. X Wang, B. Conran
Aixtron Ltd, Anderson Road, Buckingham Business Park, Swavesey, CB24 4FQ, UK

Dr. Fernan Saiz, Prof. M. Lanza
Institute of Material Science and Engineering, King Abdullah University of Science and Technology (KAUST), Thuwal 23955-6900, Saudi Arabia
E-Mail: mario.lanza@kaust.edu.sa

This article has been accepted for publication and undergone full peer review but has not been through the copyediting, typesetting, pagination and proofreading process, which may lead to differences between this version and the [Version of Record](#). Please cite this article as [doi: 10.1002/adma.202104138](https://doi.org/10.1002/adma.202104138).

This article is protected by copyright. All rights reserved.

Abstract

Two-dimensional (2D) materials have many outstanding properties that make them attractive for the fabrication of electronic devices, such as high conductivity, flexibility, and transparency. However, integrating 2D materials in commercial devices and circuits is challenging because their structure and properties can be damaged during the fabrication process. Recent studies have demonstrated that standard metal deposition techniques (like electron beam evaporation and sputtering) significantly damage the atomic structure of 2D materials. Here we show that the deposition of metal via inkjet printing technology does not produce any observable damage in the atomic structure of ultra-thin 2D materials, and that it can keep a sharp interface. These conclusions are supported by abundant data obtained via atomistic simulations, transmission electron microscopy, nano-chemical metrology, and device characterization in a probe station. Our results are important for the understanding of inkjet printing technology applied to 2D materials, and they could contribute to the better design and optimization of electronic devices and circuits.

Keywords: inkjet printing, 2D materials, hexagonal boron nitride, metal deposition, atomic defects

1 – Introduction

The market of printed electronics has reached ~7.8 billion USD in 2020, and this number is expected to raise to ~20.7 billion USD by 2025 [1]. This growth is being boosted by the relentless demand for mobile, flexible, transparent, and biocompatible electronic circuits (such as displays, solar cells, lighting, radiofrequency identifiers, sensors) [1], which cannot be fabricated using traditional materials and methods [2], such as those often employed in the complementary metal-oxide-semiconductor technology [3]. The main advantage of inkjet printing is that it can deposit different materials (such as metals [4], two-dimensional [2D] materials [5], perovskite [6], and biomaterials [7]) on multiple types of substrates (including paper [8], polymers [9], ceramic [10], and skin [11]) at a large scale and low cost. Inkjet printing is limited by the minimum line width that standard printers can reach (~5 μm), meaning that it cannot be employed for the fabrication of ultra-scaled devices (e.g., microprocessors with billions of transistors [12]). However, as mentioned, the market of electronic products that does not require such a high integration density is still big and growing, meaning that understanding and optimization of inkjet printing processes is important. More sophisticated inkjet-printers based on honed probes for scanning probe microscopes managed to print lines with widths ~15 nm [13], which is being very useful for the fabrication of prototypes for fundamental research.

Recent studies have presented the fabrication of electronic devices and circuits using inkjet-printed 2D materials, such as photodetectors and read-only memories [14]. In these cases, the devices are formed by films with thicknesses >50 nm that contain a mesh of 2D

nanosheets with mixed orientations and defective junctions between them [15]. These non-idealities limit the properties of the materials and the devices, e.g., the maximum mobility and current on/off ratios achieved in transistors with inkjet-printed MoS₂ channels are only $\sim 0.5 \text{ cm}^2 \text{ V}^{-1} \text{ s}^{-1}$ and ~ 100 [16-17], while similar devices fabricated using other industry-compatible methods, such as chemical vapour deposition (CVD), reached $\sim 10 \text{ cm}^2 \text{ V}^{-1} \text{ s}^{-1}$ and $\sim 10^8$ [18]. Moreover, the high surface roughness (root mean square $> 3 \text{ nm}$ [19]) and inhomogeneities within the inkjet-printed films result in a high device-to-device variability of the figures-of-merit of the devices [20]. For this reason, recent studies employed CVD to synthesize the 2D material and inkjet printing technology to deposit the metallic interconnections. Reference [8] fabricated field effect transistors for logic gates using monolayer and few-layers-thick CVD-grown MoS₂ as channel and inkjet-printed dielectric and interconnections, and it achieved mobilities up to $26 \text{ cm}^2 \text{ V}^{-1} \text{ s}^{-1}$ and current on/off ratios up to 50,000.

However, the use of ultra-thin 2D materials brings associated other concerns. Two recent studies have shown that the evaporation of Au on the surface of MoS₂ generates high density of atomic defects at the surface, which results in metal diffusion, metal-induced gap states, chemical bonding, and formation of interface dipoles [21-22]. The alternative proposed in that study was to transfer metal electrodes using a polymer scaffold, which is unfeasible for the wafer-scale fabrication of ultra-scaled ($< 100 \text{ nm}$) devices due to the difficult alignment and introduction of impurities from the polymer [23, 24]. It is worth noting that one layer of MoS₂ contains three rows of atoms and is $\sim 0.7 \text{ nm}$ thick [25], meaning that the damage induced by this technique may be even higher in other 2D-LMs

with monoatomic thickness (~ 0.33 nm) like graphene and h-BN. When using sputtering (a cheaper technique and therefore more widespread in academia), the damage introduced to the surface of the 2D-LMs may be even higher, due to the larger energy used during deposition. So far, the effect of metal deposition by inkjet-printing on the structure and properties of ultra-thin 2D materials has never been explored.

In this article, we exhaustively analyse the damage introduced by three different metal deposition techniques (electron beam evaporation, sputtering and inkjet printing) in the morphology of ~ 18 -layers-thick (i.e., ~ 6 nm) h-BN stacks fabricated by mechanical exfoliation and chemical vapour deposition. We selected this material because the damage introduced may have a higher effect than in any other 2D-LM, as h-BN is used as dielectric to block/modulate out-of-plane current [26-27] and in this direction atomic defects increase the leakage current exponentially [28] —i.e., the out-of-plane current in h-BN will be more affected by local defects than the in-plane current in graphene, MXenes and 2D semiconductors. And we used this thickness because it matches that used in some of the most outstanding h-BN based devices ever reported [27, 29, 30]. Our study indicates that both electron beam evaporation and sputtering introduce high amounts of defects in the h-BN stack, especially when it is synthesized by CVD method. However, inkjet printing does not produce any observable damage in the atomic structure of the h-BN stack.

2 – Atomic structure of multilayer h-BN

We produce ~ 6 -nm-thick and ~ 30 - μm -long h-BN flakes by mechanical exfoliation and deposit them on a 300 nm SiO_2/Si wafer containing a mark (see Figure 1a-c), so that the same location can be later found in subsequent analyses via scanning electron microscopy (SEM) and transmission electron microscopy (TEM). Then, a portion of the h-BN flakes is protected using three different methods: i) by patterning a $10 \mu\text{m} \times 10 \mu\text{m}$ square of negative photoresist (Figure 1d1), ii) by transferring an Au electrode (Figure 1d2), and iii) by depositing an Ag film via inkjet printing (Figure 1d3). More details about the processes followed are given in the experimental section. Then, a ~ 17 -nm-thick Au film was deposited everywhere on the samples via electron beam evaporation, using a deposition speed of 0.52 $\text{\AA}/\text{s}$ and a power of 11%; note that these parameters are similar to those often used in other studies [31-33], and are considered to introduce low damage in the materials [34]. Figure 1f shows the optical microscope image of the h-BN flake locally protected with negative photoresist before the Au evaporation, and Figure 1g shows the optical microscope image of the h-BN flake protected with transferred Au electrode (on the top side of the flake) and with Ag ink (in the bottom side of the flake).

We analyse the morphology of the h-BN stack below the protective materials (i.e., negative photoresist, transferred electrode, and Ag ink), and outside the protection (i.e., exposed to the electron beam evaporation of ~ 17 nm Au) via cross-sectional TEM. The samples were prepared via focused ion beam (FIB), and before the cut a ~ 15 -nm-thick layer

of C (first) and a ~ 10 -nm-thick layer of Cr (second) were deposited by ion sputtering; after that, a 20- μm -long, 2- μm -wide and 1- μm -thick C pattern was deposited using the materials deposition tool inside the FIB machine to indicate the area to cut, and protect it from the cutting ion gun; Figure 1h-j shows the top-view SEM images right before each cut, where the C patterns delimitate the locations for the FIB cut. To give statistical validity to our study, we collected 14 consecutive images at each location (see most of them in the Supplementary Figures 1-6), which is amply superior to what has been presented in other studies [21, 35]. Figure 2 shows the representative cross-sectional TEM images for each sample, with the protected region in the top row and the unprotected in the bottom row. As it can be observed, for all samples the protected regions of the h-BN show nearly perfect layered structure, with the 2D layers stacked and separated 0.3 nm from each other, and both the top and bottom interfaces are very sharp and clean. This also demonstrates that the FIB cuts were done using optimal parameters, and that they did not affect the morphology of our samples —previous studies in different materials showed that FIB could amorphize crystalline materials if the parameters selected (i.e., 30 kV, 30 pA) were not optimal [36], which is not the case in our study. On the contrary, the unprotected regions of the h-BN show multiple atomic defects, especially at the top interface (see Supplementary Figure 7), proving the detrimental effect of the electron beam evaporation process in the morphology of the h-BN stack. One surprising observation is that the bottom interface between the h-BN and the SiO_2 substrate also shows

to be much more defective for the unprotected regions, even if the pristine layered structure of the h-BN stack above it has not been damaged —one would expect that if a material is damaged due to the penetration of a particle, whatever is above it gets damaged too. This observation also indicates that: i) ~6-nm-thick h-BN is not enough to block the penetration of evaporated Au atoms across the h-BN stack, and ii) that the interfaces of h-BN with adjacent materials are much more sensitive to become disordered than the crystalline intra-structure.

Similar experiments have been conducted on ~6-nm-thick h-BN samples grown by metal-organic chemical vapour deposition (MOCVD) on Al₂O₃ wafers at Aixtron Ltd (United Kingdom). To avoid inhomogeneities related to impurities and micro-roughness on the surface of the substrate [37], the Al₂O₃ wafers have been firstly exposed to an annealing step in H₂ atmosphere for 5 minutes, 750 mbar at 1180°C; this resulted in an ultra-flat surface of the Al₂O₃ with a root mean square (RMS) roughness of 117 nm, as confirmed by topographic maps collected via atomic force microscopy (see Figure 2g). After the MOCVD growth of the multilayer h-BN films, inkjet-printed Ag film has been used to protect the samples, and we discarded the other two protective materials because: i) photoresist is not conductive and it cannot be used as electrode, and ii) transferring the Au electrodes is, as mentioned, not scalable and results in poor adhesion with the substrate. The MOCVD samples with and without Ag ink electrode have been exposed to ~10-nm Cr deposition by ion sputtering. To increase contrast, additional metallic layers of C and Pt were also deposited, but these processes are not expected to have any effect in the structure of the h-BN due to the presence of the Cr film. Cross-sectional TEM images of the protected sample (see Figure 2h and

Supplementary Figure 8) show that the structure of the MOCVD h-BN is layered (as confirmed by the observation of two bright spots in the Fast Fourier Transform images of the layered regions, see Supplementary Figure 9a), but not as good as the mechanically exfoliated ones, as expected. The MOCVD samples contain multiple twin boundaries where one-layer splits in two, and its interfaces are more defective and rougher than for the mechanically exfoliated samples (see Supplementary Figure 8). It should be noted that the presence of such native defects in multilayer h-BN grown by CVD and MOCVD is normal, and other recent studies have shown similar features [27, 29, 30]. Despite some studies have shown that growing single-crystalline monolayer h-BN with very low number of defects at the wafer-level using CVD [38-39] is something possible, achieving such thing for multilayer samples still remains a big challenge. In any case, the morphology of the multilayer h-BN samples grown by MOCVD represents the state-of-the-art and, while this material is still not enough good to be employed as gate dielectric in field effect transistors [40], it has been reliably used as dielectric in memristors for true random number generators (TRNGs), non-volatile memories and artificial neural networks. On the contrary, the unprotected region of the MOCVD-grown multilayer h-BN sheet (i.e., exposed to the Cr sputtering) shows a very defective structure (see Figure 2i and Supplementary Figure 10), where the interfaces have become rough and the volume of layered h-BN is much thinner; this is further confirmed by the disappearance of the two dots in the Fast Fourier Transform image of the h-BN bulk region (see Supplementary Figure 9b). Overall, the number of defects introduced by the sputtering of Cr on the MOCVD-grown h-BN samples is much higher than the number of defects introduced by the evaporation of Au on the exfoliated samples, probably due to the

presence of local native defects in the MOCVD-grown samples, which may allow the penetration of Au atoms at lower energies.

As the temperature of the sample during the evaporation of the Au is ~ 40 °C (which is very low and does not provide enough thermal energy to the sample to produce atomic motion), the only possibility is that the morphological changes in Figures 2d-f and 2i are related to the effect of atoms impacting on the surface of the multilayer h-BN stack (see Supplementary Figure 7). This was also suggested in references [21-22] by presenting some schematic drawings; however, none of those studies conducted nano-chemical measurements nor atomistic simulations to analyze this effect. In this study we carried out both types of analyses, which are presented in sections 3 and 4.

3 – Nano-chemical characterization of h-BN

Figure 3a-f shows the cross-sectional chemical composition maps collected with X-ray spectroscopy (EDS) on the mechanically exfoliated h-BN stack protected with photoresist (i.e., at both the protected and the unprotected regions), and Figure 3g-h shows the cross-sectional chemical composition profile collected with electron energy loss spectroscopy (EELS) in the same sample. Both techniques, which are integrated in the TEM instrument, allow mapping the chemical composition of the samples with sub-nanometre resolution, but EDS is more sensitive to heavy elements like Au and Pt (it cannot detect well the lightest,

like H and He) and EELS is more sensitive to light elements like H and He (it cannot detect well the heaviest, like Au and Pt). Cross-sectional EDS maps of the sample protected with negative photoresist (Figure 3b-c) show a very strong and homogeneous N signal (from the h-BN stack) right below the C layer (from the photoresist); on the contrary, the unprotected region of that same sample (Figure 3e-f) shows that the N signal at the h-BN region is weaker, discontinuous and inhomogeneous, pointing out the clear damage of the h-BN stack. Cross-sectional EELS profiles of the protected sample (Figure 3g) show a chemical composition close to ideal, with the B and N signals overlapped and symmetric, and free of any other material. On the contrary, the h-BN stack at the unprotected regions is narrower and there is displacement of O towards the h-BN stack (see Figure 3h), consistent with the damage of the SiO₂/h-BN (bottom) interface observed in the TEM images (see Figure 2d). This observation indicates that the evaporated Au atoms that penetrate in the sample release energy to the O atoms adjacent to the h-BN stack, facilitating their migration.

These analyses have been repeated for the mechanically exfoliated h-BN stacks protected with transferred Au electrodes and inkjet-printed Ag film. In both cases, similar results have been observed (see Figure 3i and Supplementary Figures 11-12). It should be noted that the interface between the transferred Au electrode and the h-BN underneath is not as good as that for the samples protected with negative photoresist and inkjet-printed Ag film, i.e., it contains multiple voids. While some portions with reasonably good Au/h-BN adhesion

can be found (see Figure 2b), statistical analysis of the cross-sectional TEM images and comparison with the other two samples reveals a worse adhesion (see Supplementary Figure 13 and 14). This is something not mentioned in references [21-22], and that indicates that the transfer of electrodes is not only unfeasible due to scalability and alignment issues, but also due to problematic adhesion to the substrate (which may increase the device-to-device variability within a wafer).

The EDS and EELS nano-chemical analyses have been also conducted in the MOCVD-grown multilayer h-BN sample partially protected with inkjet-printed Ag film (see Supplementary Figure 15). At the protected regions the EDS maps and EELS profiles reveal strong and wide N signal. The EELS profiles show B and N signals with increasing/decreasing slopes much less steep than for the exfoliated h-BN samples, indicating the diffusion of atoms at the interfaces. Despite this observation, the Al and O signals under the h-BN overlap, indicating that these materials have no strong interaction with the h-BN stack. On the contrary, at the unprotected regions of the MOCVD-grown sample the N signal is weaker and narrower, pointing the evident damage produced by the sputtering of Cr. From the cross-sectional EELS profiles, we can also see that in the unprotected region the Al and O do not overlap, and that the content of O in the h-BN stack is higher.

4 – Atomistic simulation of defect generation in multilayer h-BN

The formation of defects in the mechanically exfoliated h-BN has been simulated using first principles calculations (see Methods section). Figure 4a shows the cross-sectional view of the atomic structure of an Au atom penetrating in a multilayer h-BN stack; each plane has a crystalline structure with the B and N atoms arranged in a hexagonal lattice. This simulation reflects what is happening in the h-BN samples prepared by mechanical exfoliation, as they are free of atomic defects (see Figures 2a-c). The Au atom moves downwards in the Z plane perpendicular to the h-BN stack. We locate the atom at 5 different positions in the X-Y plane: i) on a B atom, ii) on a N atom, iii) on an interstitial, i.e., the space between the B and N atoms, iv) on a B vacancy, and v) on a N vacancy. The top-view five locations are depicted in Figure 4b. Note that the schematics on the B atom and on the B vacancy look identical, as the Au atom masks what it is below, but in fact the schematic of the B vacancy is lacking the B atom below the Au atom; the same happens for the schematics on the N atom and on the N vacancy. We calculate the energy required to move the Au atoms downwards into the h-BN stack. The results indicate that, when there is no vacancy (see Figure 4c), the energy required to introduce an Au atom into the h-BN stack is between 14 and 16 eV, depending on the location. Interestingly, this energy is reduced to ~ 2 eV when the atom is located on a N vacancy, and when the calculation is repeated on a B vacancy the atom does not see any barrier (see Figure 4d). Dynamic information about the penetration of the Au atom at each location of the 2D layered h-BN stack is also displayed in the Supplementary Video 1. We repeated these simulations for different angles, as the Au atoms in the evaporation chamber do not always fall perpendicular to the sample. However, the

simulations (shown in Supplementary Figure 16) show that the energy required to introduce the Au atom in the h-BN does not remarkably changes with the angle.

The same type of simulation has been carried out for an h-BN location with amorphous structure (see Figure 4e). This simulation reflects what is happening in the MOCVD sample, which contains some few-atoms-wide amorphous native defects related to the materials synthesis (see Figure 2h and Supplementary Figure 17). In this case, as the structure is different in every X-Y plane (i.e., non-periodical) we repeated each simulation for 5 different locations (see error bars in Figure 4f). The results indicate that the energy required to introduce the Au atom in the local defects of the MOCVD h-BN stack is much lower than for the crystalline regions, and it never surpasses 6 eV. This observation is in line with the more severe damage observed in the MOCVD h-BN samples (Figure 2i) compared to the crystalline ones (Figure 2d-f).

All these calculations indicate that introducing a metallic Au atom in the perfect 2D layered crystalline structure of the h-BN stack is difficult, as the energy needed is >14 eV, and that the native defects and dangling bonds (i.e., specially the interfaces in exfoliated samples and the few-atoms-wide regions in MOCVD samples) are promoting the clustering of atomic defects. As the minimum energy needed to detach one atom of Au from an Au crystal (also named cohesive energy) is 3.81 eV/atom (368 kJ/mol) [41], even if the minimum energy required to initiate the evaporation is reached defects in the h-BN will be always formed during the evaporation if native defects exist. In other words, if the h-BN stack contains native defects, the formation of more defects during the evaporation is unavoidable independently of the evaporation parameters used. Figure 4a also indicates that, after the Au

atom penetrates across one h-BN layer, the hexagonal crystalline lattice of B and N atoms is recovered. This is consistent with the observation of good atomic internal structure plus a damaged bottom interface (see Figure 2d-f).

5 – Electrical characterization of h-BN devices

The degradation of the atomic structure of the h-BN stack due to the evaporation or sputtering of the top electrode is expected to increase the leakage current across it, which is a very harmful effect that impedes its use in many electronic devices (e.g., gate dielectric in capacitors, insulating film in capacitors). We statistically quantify this phenomenon by fabricating dozens of matrixes of cross-point Ag/MOCVD h-BN/Ag devices, with the top Ag electrode deposited by electron beam evaporation (Figure 5a) and ink-jet printing (Figure 5b). We measure their electrical properties in a probe station by applying ramped voltage stresses (RVS) to 40 devices, and we construct the current versus voltage (I-V) plots for all of them. Figure 5b shows the median I-V plot for devices with inkjet-printed and evaporated electrodes. The green dots indicate the leakage current read at 0.1 V, and the orange dots indicate the point at which the devices exhibit a sharp current increase, indicative that the dielectric breakdown of the h-BN has been reached. The leakage current across the devices with evaporated electrodes is in average ~100 times higher; when used as dielectric in an electronic device, this would imply a ~100 times higher power consumption. Moreover, the breakdown voltage of the devices with evaporated electrodes is remarkably lower; this indicates that, for the same type of h-BN, the use of evaporated electrodes reduces the

reliability and lifetime of the device. The observation of a higher breakdown current is also indicative of a much higher power consumption before the dielectric breakdown is triggered.

Finally, we investigate the potential use of Ag/h-BN/Au devices as entropy source for TRNG circuits [29]. To do so, we expose the devices with both evaporated and inkjet-printed top electrodes to constant voltage stresses and record the current signal searching for random telegraph noise (RTN) [42]. RTN is a flagship figure-of-merit of metal/insulator/metal structures that consists on the observation of random transitions between two current states (due to stochastic charge trapping and de-trapping in the dielectric), and that enables their use as entropy source in TRNG circuits (if it is enough stable over time). Our experiments indicate that the devices with inkjet-printed top Ag electrodes readily exhibit RTN, and that it is stable for long periods of time. Figure 5g shows a portion of the RTN characteristic measured. As it can be observed, both current levels can be clearly distinguished, something that it is even more clear in the weighted time lag plot presented in Figure 5h. Therefore, the Ag/h-BN/Au devices using top Ag electrodes not only exhibit less leakage and breakdown current (see Figures 5c-f), but also the presence of an additional electronic phenomena (i.e., RTN) that enables their use in other applications (i.e., entropy source in TRNG circuits).

6 – Conclusions

In conclusion, we have analysed the effect of metal deposition techniques on the morphology and structure of multilayer h-BN. Cross-sectional TEM images of mechanically exfoliated h-BN samples show a nearly perfect atomic structure and sharp interfaces under

the TEM, but when it is exposed to electron beam evaporation of ~ 17 nm Au the interfaces with adjacent materials become diffuse and the internal structure becomes highly defective. Moreover, the EELS and EDS nano-chemical analyses reveal the presence of O impurities in the samples. These phenomena are aggravated in MOCVD-grown h-BN samples exposed to sputtering of Cr, probably due to the higher density of native defects (which reduces the mechanical and chemical stability of the h-BN film). Finally, we discovered that inkjet printing is a very practical method to deposit metals (in our study Ag) without damaging the structure of the h-BN stack, which results in lower leakage/breakdown currents and the observation of stable RTN.

Experimental Section

Mechanically exfoliated h-BN samples: 300 nm SiO₂/n-Si wafers were cut into 1.5 cm \times 1.5 cm pieces and ultrasonic bathed (power 99 W) in acetone, alcohol and deionized water for 20 min, respectively. A 10 μ m \times 10 μ m squared Au as a mark was fabricated by standard photolithography using a mask aligner (SUSS MJB4) and an electron beam evaporator (PVD 75, Kurt J. Lesker). The exfoliated h-BN flakes have been peeled off from bulk h-BN crystal (HQ graphene) using tape (SPV-224PR, Nitto), are transferred using polydimethylsiloxane (PDMS) (WF-30-x4-6mil, Gel-park) on the cleaned 300 nm SiO₂/n-Si substrates using a transfer stage (OWTS-01, Shanghai ONWAY Technology Co., Ltd) doted with an optical microscope. The transfer stage allowed placing the flakes at the wanted position, and the flakes were deposited near to the pre-patterned 10 μ m \times 10 μ m squared Au mark. Then, the

h-BN was protected in three ways: i) a small $10\ \mu\text{m} \times 10\ \mu\text{m}$ square of negative photoresist (GM1040, SU8) was patterned on the h-BN flake by photolithography using a mask aligner (SUSS MJB4). The negative photoresist was spin coated on the exfoliated h-BN flake and substrate, and then baked at $120\ ^\circ\text{C}$ for 3 min; the surface of the sample was selectively exposed to ultraviolet light ($10\ \text{mW}/\text{cm}^2$) for 1.6 s using a glass mask, baked at $120\ ^\circ\text{C}$ for 25 seconds, and immersed liquid PGMEA ($\text{C}_6\text{H}_{12}\text{O}_3$) for 10 s to remove the parts of the negative photoresist that were not exposed to light. The thickness of the squared negative photoresist protecting the h-BN was $\sim 1\ \mu\text{m}$, as confirmed using a profilometer. ii) Au electrodes were transferred on the h-BN flakes using a transfer stage. The Au electrodes were first fabricated by photolithography and electron beam evaporator on cleaned $300\ \text{nm}\ \text{SiO}_2/\text{n-Si}$ substrates, and exfoliated using PDMS fit tape as scaffold. The width and thickness of Au electrode are $5\ \mu\text{m}$ and $60\ \text{nm}$ respectively. iii) Ag ink (Jet-600C, Hisense) was printed on the h-BN flakes using an inkjet printer (DMP-2800, FUJIFILM Dimatix), using Dimatix Drop Manager describe parameters $10\ \text{pL}$ (one drop). After the protections, a layer of $17\ \text{nm}$ Au was deposited by electron beam evaporator on all the samples, covering both protected and unprotected regions, using a rate of $0.52\ \text{\AA}/\text{s}$ and a power of 11%. All the Au evaporations in this study were carried out under a vacuum atmosphere of 6.75×10^{-5} torr. Before the TEM images, the samples were covered with a layer of $\sim 15\ \text{nm}$ -thick-C (first) and $\sim 10\ \text{nm}$ -thick-Cr (second) using an ion beam coater (681, 682, GATAN).

MOCVD h-BN samples: The h-BN is grown directly on c-plane Al_2O_3 (0001) surface at $1400\ ^\circ\text{C}$, $500\ \text{mbar}$ for 30 minutes in AIXTRON CCS 2D reactor. The borazine is used as the single source precursor in the growth. Prior to h-BN growth, the sapphire substrates are

annealed in the same reactor in H_2 atmosphere. After the growth, Ag ink (Jet-600C, Hisense) was printed on the h-BN flakes using an inkjet printer (DMP-2800, FUJIFILM Dimatix), using Dimatix Drop Manager describe parameters 10 pL (one drop). Before the TEM images, sample 4 (inkjet-printed Ag/MOCVD h-BN/ Al_2O_3) was covered with layers of ~ 15 nm-thick-C (first), and ~ 10 nm-thick-Cr (second) using an ion beam coater (681, 682, GATAN). For sample 5 (MOCVD h-BN/ Al_2O_3) it was the opposite order of evaporation. An additional layer of ~ 6 nm-thick-Pt was deposited on top using an ion sputter coater (E-1030, HITACHI).

Materials characterization: Optical microscope images of the samples are taken using a polarizing microscopy (Leica DM400). The cross-sectional TEM images of the samples were taken as follows: i) an FIB (HELIOS NANOLAB 450S, FEI) was used to cut the samples into thin lamellas; ii) the thin lamellas were placed in the TEM grid using a micromanipulator; iii) the samples were analysed in a high-resolution TEM (JEM-2100, FEI) working at 200 KV. EDS data and EELS data are obtained using the setup integrated in the TEM machine.

Device fabrication and characterization: The bottom electrodes Bottom electrodes consisting on 40 nm Ag on 3 nm Ti were patterned using a mask aligner (SUSS MJB4) and an electron beam evaporator (PVD 75, Kurt J. Lesker). Then, the CVD h-BN has been transferred on the bottom electrodes following a well-known wet transfer process using PMMA as scaffold [43]. The evaporated top Ag electrodes were constructed using the same process than the bottom ones (but without Ti), and the inkjet-printed top Ag electrodes were printed using inkjet printer (DMP-2800, FUJIFILM Dimatix). The electrical properties of the

devices were measured in a Cascade probe station (model M150) connected to a semiconductor parameter analyser (4200-SCS, Keithley).

First-principles calculations: We use a first-principles methodology that is composed of four steps. In the first step, we build five layers of hexagonal boron nitride by replicating the unit cell 5×5 times, accounting for 250 atoms. We add a vacuum gap of 1.7 nm in the z-direction to create two surfaces followed by a geometry relaxation during which the positions and cell parameters of the five layers are relaxed using the Vienna Ab initio Package (VASP) [44-46]. Reciprocal space integrations in VASP are calculated at the Γ point in the Brillouin zone. The geometry relaxation is carried out setting thresholds of 0.2 eV/nm for the forces and 1.0×10^{-5} eV for the self-consistency solution of the wavefunction. We use generalized-gradient approximation (GGA) for the exchange-correlation potential in the Perdew-Burke-Ernzerhof (PBE) [47] parameterization and the projector augmented wave method (PAW) [48]. We expand the valence orbitals with a plane wave basis with an energy cut-off of 350 eV after a convergence test of the total energy. Long-range van der Waals forces are included using the Zero damping Grimme's DFT-D3 scheme [49]. We choose this scheme because it gives a better agreement with bulk lattice parameters with respect to other descriptions of the van der Waals forces available in VASP. This DFT recipe has been validated in our recent work on the formation of B vacancies in boron nitride.

The second step is to place an Au atom in the simulation box above the relaxed h-BN layers with a distance of 0.72 nm apart from the upper nanosheet and is aligned to a B atom. We then relax again the positions of the whole system, keeping a constraint in which fixed the positions of the Au atom and the lowest-lying layer. In the third step, we keep applying

this constraint when running 60 simulations in which the Au atom is moved towards the BN structure by $\Delta z = 0.025$ nm in each one. As a result, this metal ion is able to penetrate across the fourth layer at the end of the 60th run. In each i th run, this ion's position is $z = i \cdot \Delta z$ and we calculate the associated migration energy $E_{mig} [z]$ from initial position z_0 to as:

$$E_{mig} [z] = E_{tot} [z] - E_{tot} [z_0], \quad (1)$$

where the $E_{tot} [z]$ and $E_{tot} [z_0]$ are the system's total energies for each z and the initial z_0 given by VASP.

In addition to having the Au aligned to a B particle, we also simulate other situations, where the displaced ion impacts on a N atom and a interstitial space in the upper layer. We also calculate the migration energies when the aforementioned B and N atoms are vacant and when the angle of incidence α is 10, 20, 30, and 40 degrees by applying the corresponding displacement Δx along the x-axis in each run.

Finally, we compare the migration energies obtained with the implantation of one isolated Au atom in the vacuum with those when this particle is initially located in a semi-infinite golden slab that is contact with another one made of amorphous boron nitride (a-BN). The Au slab is generated by cleaving the fcc structure in the (111) direction using the ASE package [50]. Upon this cleavage the Au slab has a thickness of four atoms and a cross section with a parallelogram shape whose cell vectors are $a = b = 1.44$ nm and angles $\alpha = \beta = 90$ degrees and $\gamma = 120$ degrees to assemble the a-BN solid. This solid is generated employing the following procedure based on ab initio molecular dynamics (AIMD) to

generate liquid structures for others materials with high melting points such as silicon carbide [51]. First, we melt five h-BN nanosheets up to 4300 K in 20000 AIMD steps at constant volume. At the beginning of the AIMD calculation, the volume of this simulation box is adjusted to match the experimental density of 2.28 g/cm^3 of amorphous boron nitride (a-BN). The molten is then quenched to 300 K with 20000 AIMD steps, each one with a length of 0.5×10^{-3} ps. We next add a vacuum gap of 1.2 nm in the z-direction to create two surfaces and carry out a geometry relaxation of the positions at constant volume during which atoms in the surface rearrange. Finally, the Au and a-BN slabs are placed in contact with a vacuum gap of around 1.8 nm to then relax the atomic positions and cell vectors of the resulting interfacial system to minimize lateral strains in the x and y directions. Due to the disordered structure of the a-BN layer, the migration energies for all 60 simulations are calculated averaging the values obtained with displacing five different atoms departing from the lower face of the metallic slab.

Acknowledgement

This work has been supported by the Baseline funding scheme of the King Abdullah University of Science and Technology (KAUST), the Ministry of Science and Technology of China (grants no. 2018YFE0100800, 2019YFE0124200), the National Natural Science Foundation of China (grants no. 61874075), the Suzhou Science and Technology Bureau, the Ministry of Finance of China (grant no. SX21400213), the 111 Project from the State Administration of Foreign Experts Affairs of China, the Collaborative Innovation Centre of

Suzhou Nano Science & Technology, the Jiangsu Key Laboratory for Carbon-Based Functional Materials & Devices, and the Priority Academic Program Development of Jiangsu Higher Education Institutions. For computer time, this research used the resources of the Supercomputing Laboratory at King Abdullah University of Science & Technology (KAUST) in Thuwal, Saudi Arabia.

References

- [1] Printed Electronics Market worth \$20.7 billion by 2025, <https://www.marketsandmarkets.com/PressReleases/printed-electronics-market.asp>
- [2] W. Wu, *Nanoscale*, **2017**, 9, 7342-7372.
- [3] C. -X. Xue, Y. -C. Chiu, T. -W. Liu¹, T. -Y. Huang, J. -S. Liu, T. -W. Chang, H. -Y. Kao, J. -H. Wang, S. -Y. Wei, C. -Y. Lee, S. -P. Huang, J. -M. Hung, S. -H. Teng, W. -C. Wei, Y. -R. Chen, T. -H. Hsu, Y. -K. Chen, Y. -C. Lo, T. -H. Wen, C. -C. Lo, R. -S. Liu, C. -C. Hsieh, K. -T. Tang, M. -S. Ho, C. -Y. Su, C. -C. Chou, Y. -D. Chih, M. -F. Chang, *Nat Electron*, **2021**, 4, 81-90.
- [4] A. Kamyshny, J. Steinke, S. Magdassi, *Open Appl. Phys. J*, **2011**, 4, 19-36.
- [5] T. Carey, S. Cacovich, G. Divitini, J. Ren, A. Mansouri, J. M. Kim, C. Wang, C. Ducati, R. Sordan, Felice Torrisi, *Nat Commun*, **2017**, 8, 1202.
- [6] X. Peng, J. Yuan, S. Shen, M. Gao, A. S. R. Chesman, H. Yin, J. Cheng, Q. Zhang, D. Angmo, *Adv Funct Mater*, **2017**, 27, 1703704.

- [7] X. Li, B. Liu, B. Pei, J. Chen, D. Zhou, J. Peng, X. Zhang, W. Jia, T. Xu, *Chem Rev*, **2020**, 120, 19, 10793-10833.
- [8] S. Conti, L. Pimpolari, G. Calabrese, R. Worsley, S. Majee, D. K. Polyushkin, M. Paur, S. Pace, D. H. Keum, F. Fabbri, G. Iannaccone, M. Macucci, C. Coletti, T. Mueller, C. Casiraghi, G. Fiori, *Nat Commun*, **2020**, 11, 3566.
- [9] X. Nie, H. Wang, J. Zou, *Appl Surf Sci*, **2012**, 261, 554-560.
- [10] S. G. Kirtania, M. A. Riheen, S. U. Kim, K. Sekhar, A. Wisniewska, P. K. Sekhar, *Micromachines*, **2020**, 11, 841.
- [11] Y. Yu, J. Zhang, Jing Liu, *PLoS ONE*, **2013**, 8(3), e58771.
- [12] D. Patel, Apple's A14 Packs 134 Million Transistors/mm², but Falls Short of TSMC's Density Claims. *Semi Analysis*. (accessed on January 13th 2021).
- [13] T. Yeshua, M. Layani, R. Dekhter, U. Huebner, S. Magdassi, A. Lewis, *Small*, **2017**, 1702324.
- [14] D. McManus, S. Vranic, F. Withers, V. Sanchez-Romaguera, M. Macucci, H. Yang, R. Sorrentino, K. Parvez, S. Son, G. Iannaccone, K. Kostarelos, G. Fiori, C. Casiraghi, *Nat Nanotechnol*, **2017**, 12, 343-350.
- [15] X. Feng, Y. Li, L. Wang, S. Chen, Z. G. Yu, W. C. Tan, N. Macadam, G. Hu, L. Huang, L. Chen, X. Gong, D. Chi, T. Hasan,* A. V. -Y. Thean,* Y. -W. Zhang, K. -W. Ang, *Adv. Electron. Mater*, **2019**, 5, 1900740.
- [16] A. G. Kelly, T. Hallam, C. Backes, A. Harvey, A. S. Esmaily, I. Godwin, J. Coelho, V. Nicolosi, J. Lauth, A. Kulkarni, S. Kinge, L. D. A. Siebbeles, G. S. Duesberg, J. N. Coleman, *Science*, **2017**, 356, 69-73.

- [17] A. G. Kelly, V. Vega-Mayoral, J. B. Boland, J. N. Coleman, *2D Mater*, **2019**, 6, 045036.
- [18] H. Kwon, S. Garg, J. H. Park, Y. Jeong, S. Yu, S. M. Kim, P. Kung, S. Im, *NPJ 2D Mater. Appl*, **2019**, 3, 9.
- [19] Y. -L. Hsieh, W. -H. Su, C. -C. Huang, C. -Y. Su, *Nanotechnology*, **2019**, 30, 445702.
- [20] M. Lanza, Q. Smets, C. Huyghebaert, L. -J. Li, *Nat Commun*, **2020**, 11, 5689.
- [21] Y. Liu, J. Guo, E. Zhu, L. Liao, S. J. Lee, M. Ding, I. Shakir, V. Gambin, Y. Huang, Y. Liu, X. Duan, *Nature*, **2018**, 557, 696-700.
- [22] L. Liu, L. Kong, Q. Li, C. He, L. Ren, Q. Tao, X. Yang, J. Lin, B. Zhao, Z. Li, Y. Chen, W. Li, W. Song, Z. Lu, G. Li, S. Li, X. Duan, A. Pan, L. Liao, Y. Liu, *Nat Electron*, **2021**, 4, 342-347.
- [23] J.D. Wood, G.P. Doidge, E.A. Carrion, J.C. Koepke, J.A. Kaitz, I. Datye, A. Behnam, J. Hewaparakrama, B. Aruin, Y. Chen, H. Dong, R.T. Haasch, J.W. Lyding, E. Pop, *Nanotechnology*, **2015**, 26, 055302.
- [24] Z. Wang, Z. Zhang, Electron Beam Evaporation Deposition. In: Y. Lin, X. Chen. eds. *Advanced Nano Deposition Methods*. **2016**, 33-58.
- [25] R. Frisenda, M. Drüppel, R. Schmidt, S. M. de Vasconcellos, D. P. de Lara, R. Bratschitach, M. Rohlfing, *npj 2D Mater Appl*, **2017**, 1, 10.
- [26] F. Hui, C. Pan, Y. Shi, Y. Ji, E. Grustan-Gutierrez, M. Lanza, *Microelectron Eng*, **2016**, 163, 119-133.
- [27] X. -T. Liu, J. -R. Chen, Y. Wang, S. -T. Han, Y. Zhou, *Adv. Funct. Mater*, **2020**, 31, 2004733.

- [28] F. -C. Chiu, *Adv. Mater. Sci. Eng.*, **2014**, 2014, 1-18.
- [29] C. Wen, X. Li, T. Zanotti, F. M. Puglisi, Y. Shi, F. Saiz, A. Antidormi, S. Roche, W. Zheng, X. Liang, J. Hu, S. Duhm, J. B. Roldan, T. Wu, V. Chen, E. Pop, B. Garrido, K. Zhu, F. Hui, M. Lanza*, *Adv. Mater.*, **2021**, 2100185.
- [30] S. Chen, M. R. Mahmoodi, Y. Shi, C. Mahata, B. Yuan, X. Liang, C. Wen, F. Hui, D. Akinwande, D. B. Strukov, M. Lanza, *Nat. Electron*, **2020**, 3, 638-654.
- [31] M. Wang, S. Cai, C. Pan, C. Wang, X. Lian, Y. Zhou, K. Xu, T. Cao, X. Pan, B. Wang, S. -J. Liang, J. J. Yang, P. Wang, F. Miao, *Nat. Electron*, **2018**, 1, 130-136.
- [32] C. Pan, C. -Y. Wang, S. -J. Liang, Y. Wang, T. Cao, P. Wang, C. Wang, S. Wang, B. Cheng, A. Gao, E. Liu, K. Watanabe, T. Taniguchi, F. Miao, *Nat. Electron*, **2020**, 3, 383-390.
- [33] X. Wu, R. Ge, Y. Huang, D. Akinwande, J. C. Lee, *RSC Adv.*, **2020**, 10, 42249-42255.
- [34] Kurt J. Lesker Company. Gold (Au) Pellets Evaporation Materials. Available from https://www.lesker.com/newweb/deposition_materials/depositionmaterials_evaporatio_nmaterials_1.cfm?pgid=au1
- [35] C. M. Went, J. Wong, P. R. Jahelka, M. Kelzenberg, S. Biswas, M. S. Hunt, A. Carbone, H. A. Atwater, *Sci. Adv.*, **2019**, 5, eaax6061.
- [36] A. B. Andersen, A. Shivayogimath, T. Booth, S. Kadkhodazadeh, T. W. Hansen, *Phys. Status Solidi*, **2020**, 257, 2000318.
- [37] Y. Shi, B. Groven, J. Serron, X. Wu, A. N. Mehta, A. Minj, S. Sergeant, H. Han, I. Asselberghs, D. Lin, S. Brems, C. Huyghebaert, P. Morin, I. Radu, M. Caymax, *ACS Nano*, **2021**, 15, 6, 9482-9494.

- [38] T. -A. Chen, C. -P. Chuu, C. -C. Tseng, C. -K. Wen, H. -S. Philip Wong, S. Pan, R. Li, T. -A. Chao, W. -C. Chueh, Y. Zhang, Q. Fu, B. I. Yakobson, W. -H. Chang, L. -J. Li, *Nature*, **2020**, 579, 219–223.
- [39] J. S. Lee, S. H. Choi, S. J. Yun, Y. I. Kim, S. Boandoh, J. -H. Park, B. G. Shin, H. Ko, S. H. Lee, Y. -M. Kim, Y. H. Lee, K. K. Kim, S. M. Kim, *Science*, **2018**, 362, 817-821.
- [40] T. Knobloch, Y. Y. Illarionov, F. Ducry, C. Schleich, S. Wachter, T. Knobloch, Y. Y. Illarionov, F. Ducry, C. Schleich, S. Wachter, T. Müller, M. Walzl, M. Lanza, M. I. Vexler, M. Luisier, T. Grasser, *Nat. Electron*, **2021**, 4, 98-108.
- [41] Charles Kittel. Introduction to Solid State Physics, 8th edition. Hoboken, NJ: *John Wiley & Sons, Inc.*, **2005**.
- [42] X. Li, T. Zanotti, T. Wang, K. Zhu, F. M. Puglisi, M. Lanza, *Adv. Func. Mater*, **2021**, 31, 2102172.
- [43] Yuanyuan Shi, Xianhu Liang, Bin Yuan, Victoria Chen, Haitong Li, Fei Hui, Zhouchangwan Yu, Fang Yuan, Eric Pop, H.-S. Philip Wong, Mario Lanza*, *Nat. Electron*, **2018**, 1, 458–465.
- [44] G. Kresse, J. Hafner, *Phys. Rev. B*, **1993**, 47, 558.
- [45] G. Kresse, J. Furthmüller, *Comp. Mat. Sci*, **1996**, 6, 15.
- [46] G. Kresse, J. Furthmüller, *Phys. Rev. B*, **1996**, 54, 11169.
- [47] J. P. Perdew, K. Burke, M. Ernzerhof, *Phys. Rev. Lett*, **1996**, 77, 3865.
- [48] G. Kresse, D. Joubert, *Phys. Rev. B*, **1999**, 59, 1758.
- [49] S. Grimme, J. Antony, S. Ehrlich, H. Krieg, *J. Chem. Phys*, **2010**, 132, 154104.

- [50] A. H. Larsen, J. J. Mortensen, J. Blomqvist, I. E. Castelli, R. Christensen, M. Dulak, J. Friis, M. N. Groves, B. Hammer, C. Hargus, *J. Phys.: Condens. Matter*, **2017**, 29, 273002.
- [51] F. Saiz, *J. Phys. Chem. Solid*, **2020**, 137, 109204.

List of Figures

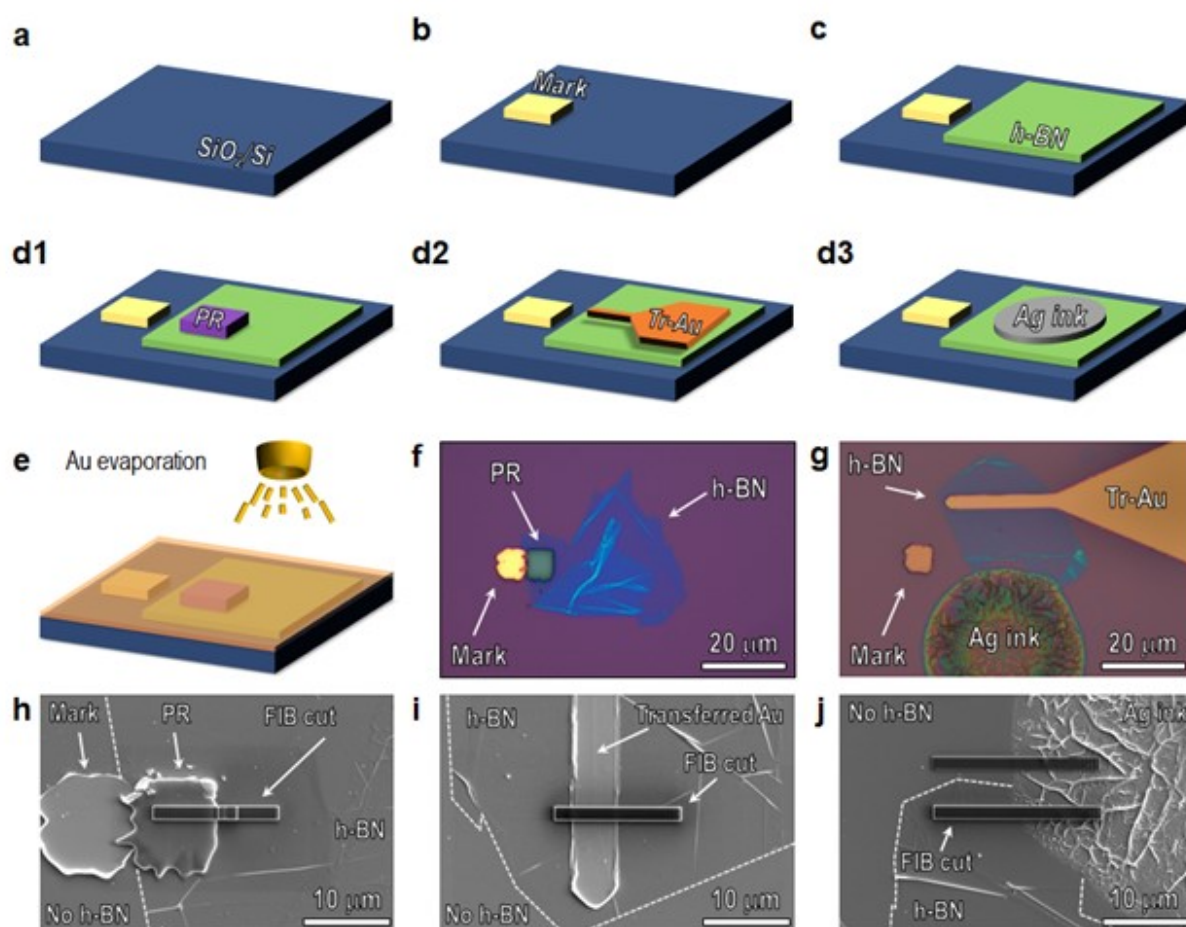


Figure 1. Illustration and structure of three protection methods. (a) Clean SiO₂/Si substrate. (b) Electron-beam-deposited Au on clean SiO₂/Si substrate as a mark. (c) Mechanically exfoliated h-BN flake was transferred on clean SiO₂/Si substrate. (d.1) ME h-BN protected with negative photoresist. (d.2) Transferred Au electrode as a protection layer on ME h-BN. (d.3) Ag ink was inkjet-printed on ME h-BN. (e) 17 nm Au was deposited on three samples after fabrication. (f) Optical image of sample 1. (g) Optical image of sample 2 and 3. (h) SEM image of FIB cut region of sample 1. (i) SEM image of FIB cut region of sample 2. (j) SEM image of FIB cut region of sample 3.

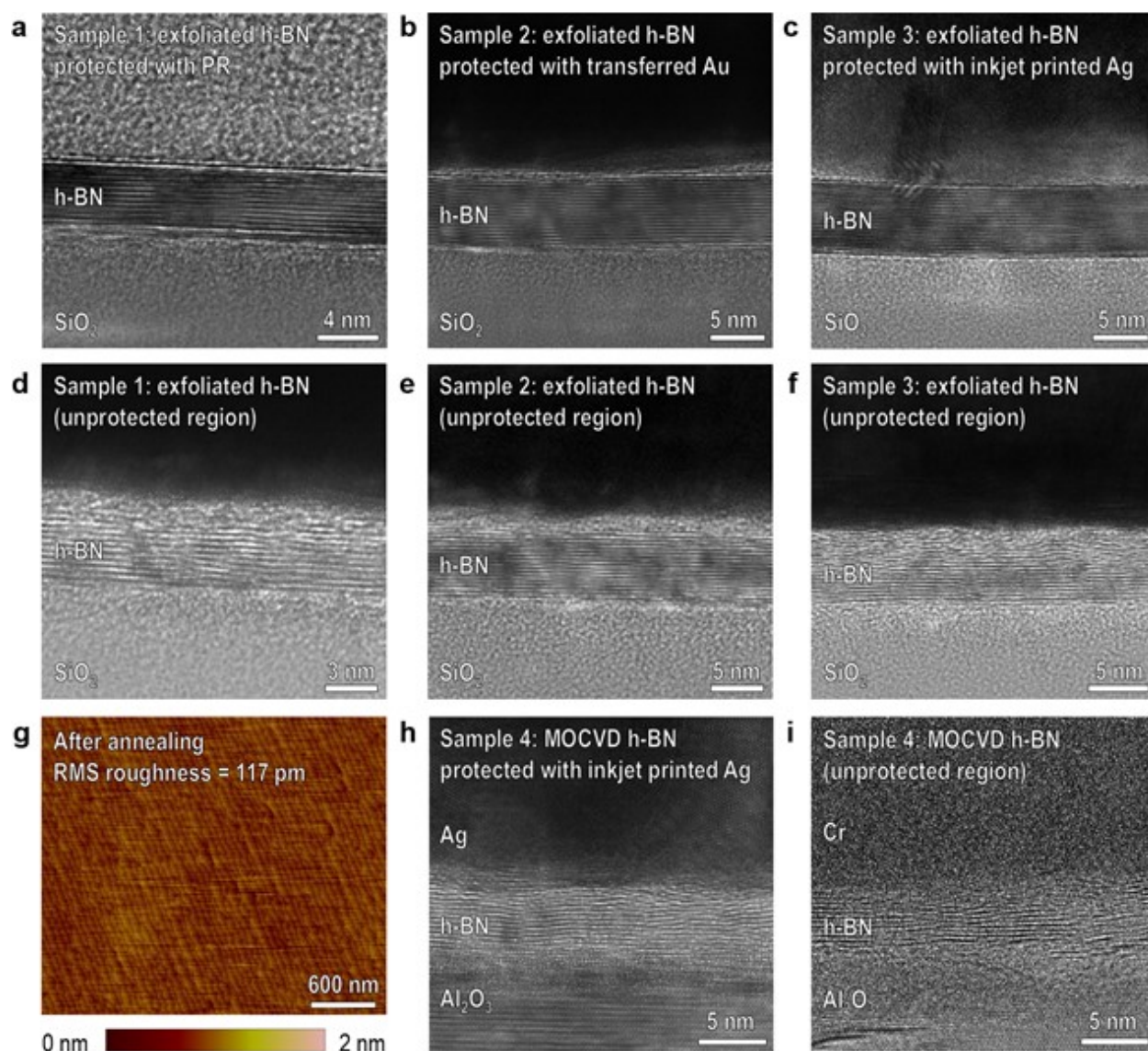


Figure 2. Morphological characterizations of exfoliated h-BN. (a) TEM image of sample 1 protected by negative photoresist, with well-defined interface. (b) TEM image of sample 2 protected by transferred Au electrode, with clear metal-insulator interface. (c) TEM image of sample 3 protected by inkjet-printed Ag ink, with sharp and clean interface. (d-f) TEM images of sample 1,2,3 covered by electron-beam-deposited Au, with distorted and defects

induced interface. (g) Topographic AFM map of the surface of the Al_2O_3 after an annealing process to clean its surface, before the MOCVD growth of the multilayer h-BN sheet). (h) and (i) show the cross-sectional TEM images of the MOCVD h-BN sample after the sputtering of a Cr film at (h) a location previously protected with inkjet-printed Ag, and (i) an unprotected region.

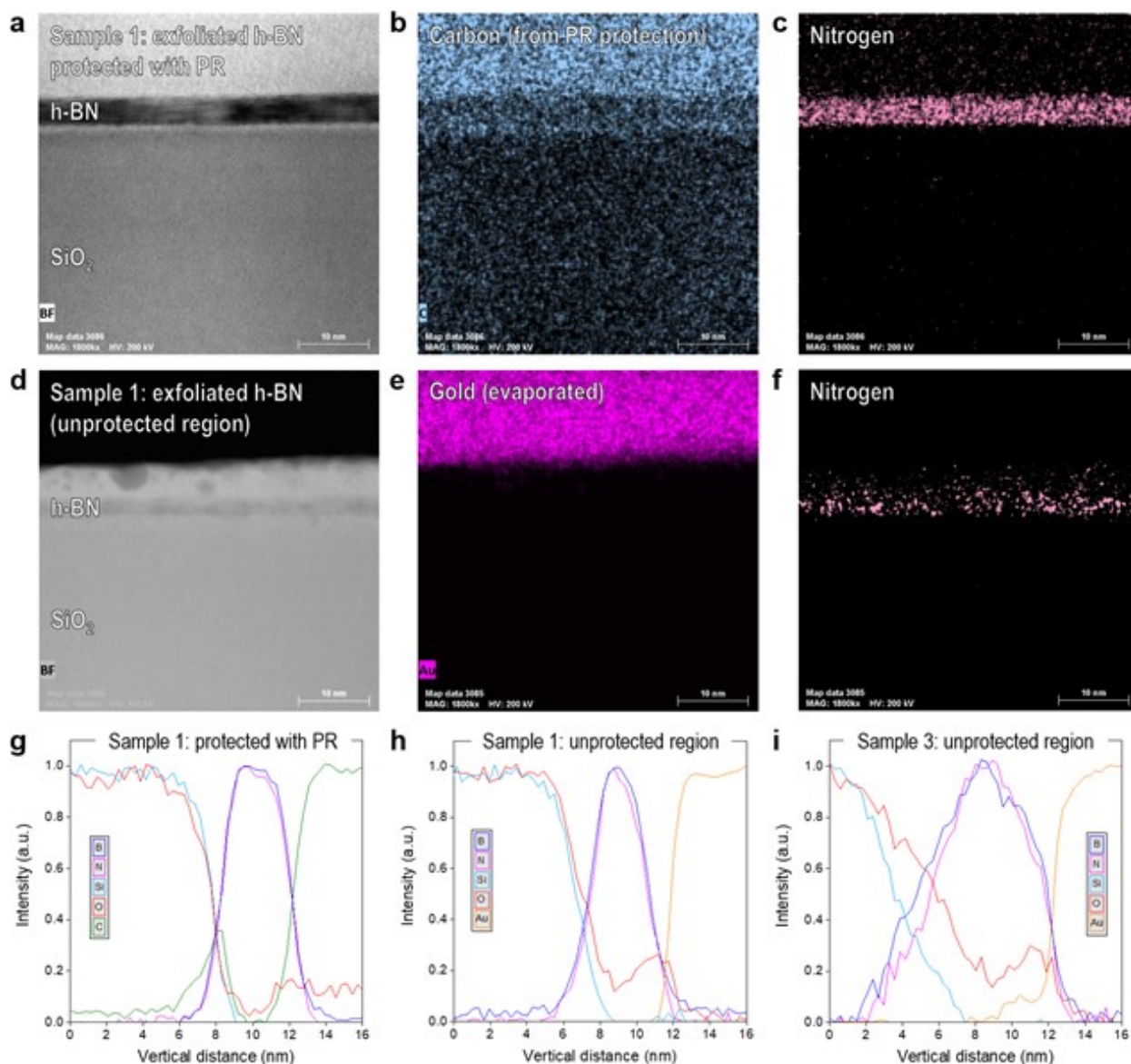


Figure 3. Nano-chemical characterization of mechanically exfoliated h-BN. (a) STEM image of the mechanically exfoliated h-BN stack with 17 nm Au evaporated on top at a location protected with photoresist. (b) and (c) EDS maps of C and N signals for the mechanically exfoliated h-BN with 17 nm Au evaporated on top stack at a region protected with photoresist. (d) STEM image of the mechanically exfoliated h-BN with 17 Au nm evaporated on top stack at an unprotected region. (e) and (f) EDS maps of Au and N signals for the mechanically exfoliated h-BN stack with 17 nm Au evaporated on top at a location protected with photoresist. (g) and (h) EELS profiles collected in a mechanically exfoliated h-BN stack with 17 nm Au evaporated on top at a location protected with photoresist and unprotected. (i) EELS profile collected in a mechanically exfoliated h-BN stack with 17 nm Au evaporated on top at a location unprotected.

location (respectively). (i) EELS profiles collected in a mechanically exfoliated h-BN stack with 17 nm Au evaporated on top at a location protected with an inkjet-printed Ag electrode.

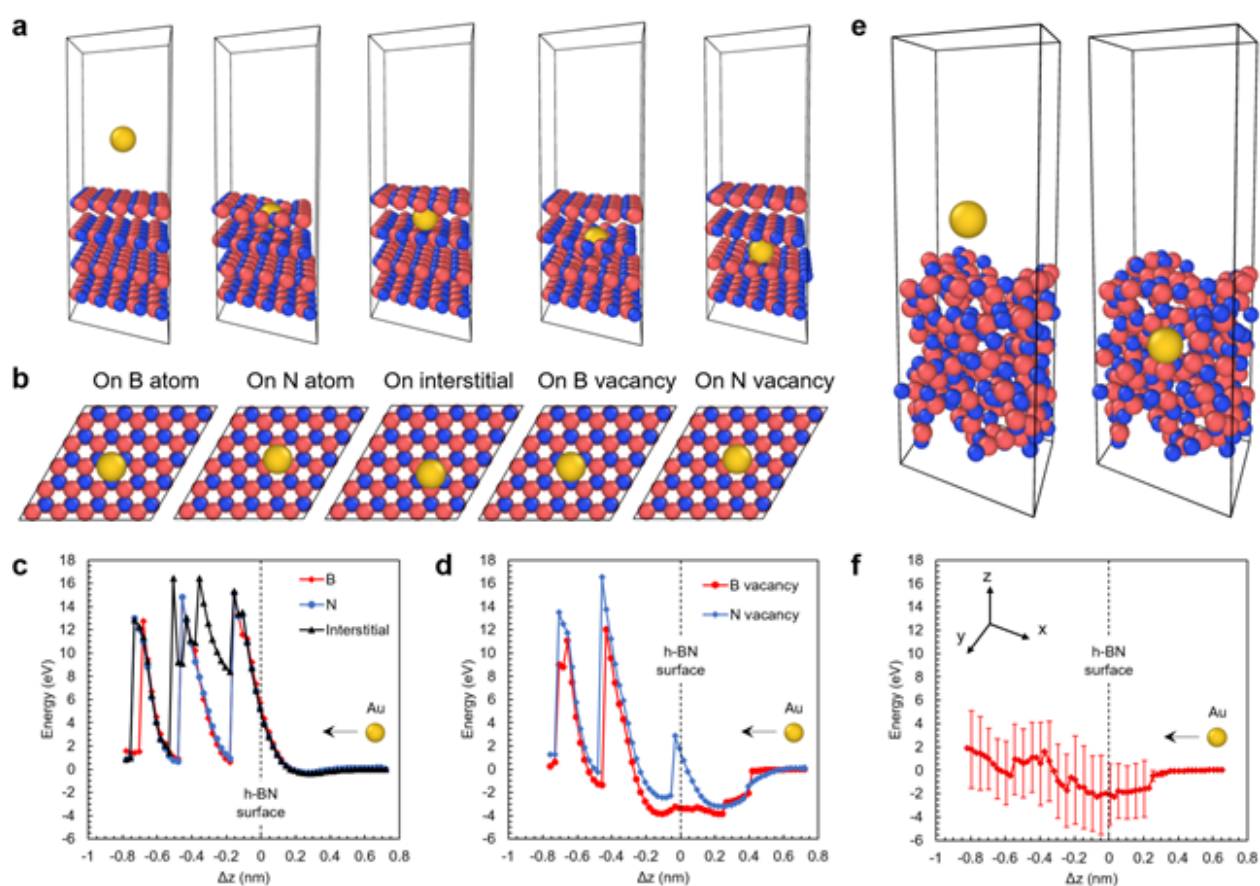


Figure 4. Atomistic simulations of Au evaporation in h-BN. (a) Cross-sectional schematic of an Au atom penetrating in a h-BN stack with perfect layered crystalline structure. (b) Top-view schematic of the five locations at which the penetration has been calculated. The top-view schematics of the vacancies look identical to the ones on the atoms, but in fact there is an B or N atom missing below (which is masked by the Au atom). (c) and (d) calculation of

the energy required to move an Au atom inside the h-BN stack (along the Z axis, at 90°C perpendicular respect to the h-BN plane) for the five different locations indicated in (b). Dynamic information about the penetration of the Au atom into the crystalline 2D layered h-BN stack at each location is shown in the Supplementary Video 1. (e) Cross-sectional schematic of a few-atoms-wide native defect in the layered MOCVD h-BN, and the penetration of an Au atom across it. (f) Energy required to move an Au atom inside the few-atoms-wide amorphous region. The error bars consider 5 calculations, each of them at a different location in the X-Y plane. The zero in panels (c), (d) and (f) indicates the surface of the h-BN stack, and the X-Y-Z axis corresponding to the entire figure are shown as inset in panel (c).

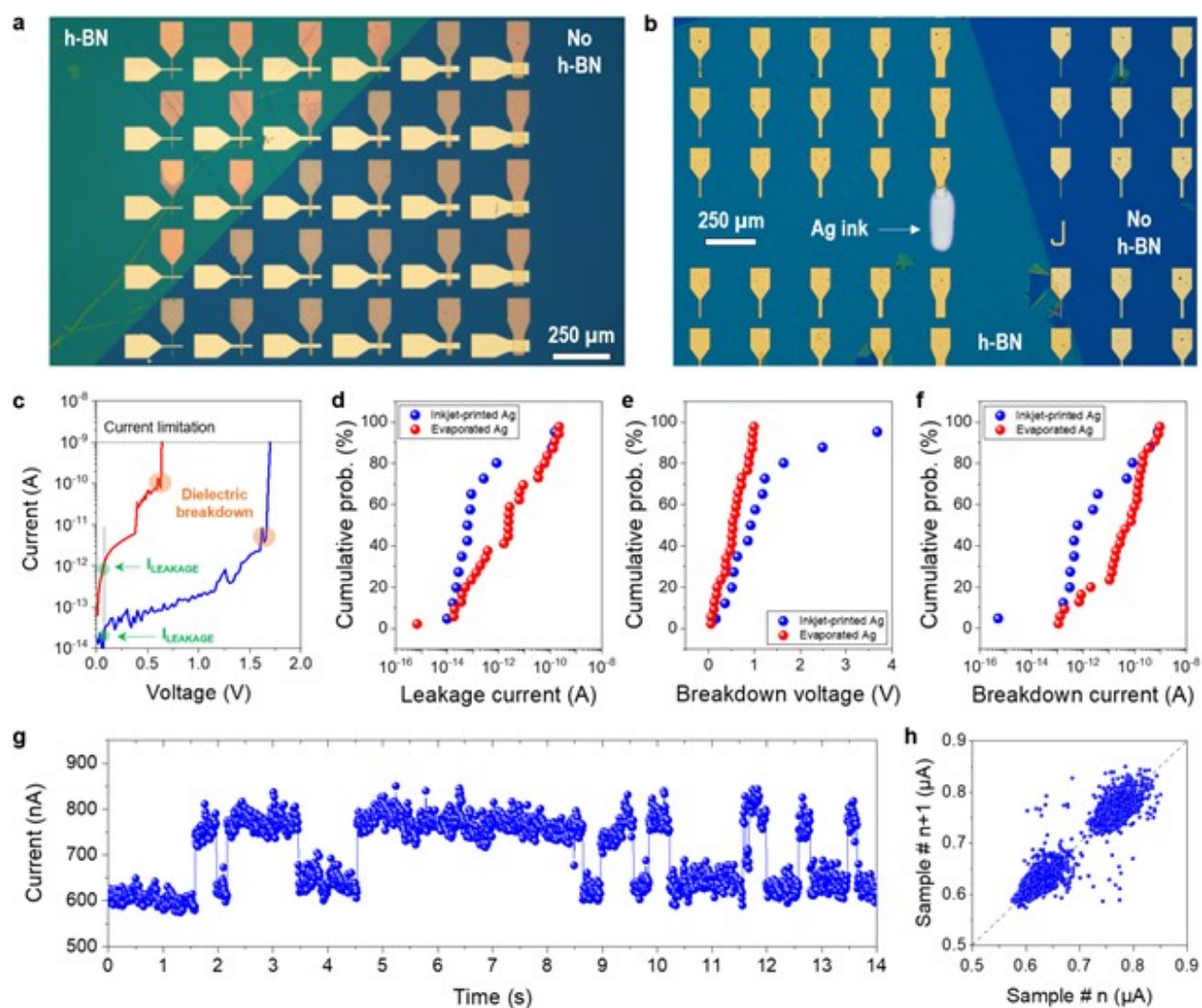


Figure 5. Electrical characterization of Ag/h-BN/Ag devices. (a) Optical microscope image of a matrix of Ag/MOCVD h-BN/Ag cross-point devices with top electrodes deposited with electron beam evaporation. (b) Optical microscope image of a Ag/MOCVD h-BN/Ag cross-point device with top electrode deposited with inkjet-printing. (c) Representative I-V curves of Ag/h-BN/Ag devices with top electrodes deposited by inkjet printing (blue) and electron beam evaporation (red). (d), (e) and (f) show the statistical analysis of the leakage current, breakdown voltage and breakdown current (respectively). (g) Stable RTN signal measured in the Ag/h-BN/Au sample with top electrode patterned via inkjet-printing when stressed at a constant voltage of 70 mV; similar structures with top Ag electrodes patterned via electron beam evaporation did not exhibit this behaviour. (h) Weighted scatter plot of the current data evaluated at the discrete time $i+1$ vs. i (i.e., consecutive current values define y- and x- axis,

respectively). This type of plot, called weighted Time Lag Plot (w-TLP), demonstrates that the currents in Figure 5g concentrate in two groups, and proves the presence of RTN.

The evaporation of Au or the sputtering of Cr on two-dimensional (2D) layered hexagonal boron nitride (h-BN) produces local atomic defects in its structure, specially at its interfaces, which increases the leakage current across it. We find that the deposition of metal on h-BN using inkjet printing does not introduce any defect, and maintains its layered structure free of defects.

